RSC Advances

COMMUNICATION

View Article Online
View Journal | View Issue

Cite this: *RSC Adv.*, 2014, **4**, 29698

Received 30th April 2014
Accepted 23rd June 2014

DOI: 10.1039/c4ra03943b

www.rsc.org/advances

Controllable growth of SnS_2/SnO_2 heterostructured nanoplates *via* a hydrothermal-assisted self-hydrolysis process and their visible-light-driven photocatalytic reduction of Cr(VI)†

Liyuan Mao,‡ Jingjing Li,‡ Yunlong Xie, Yijun Zhong and Yong Hu*

A novel and facile hydrothermal-assisted self-hydrolysis route has been proposed for the controllable preparation of SnS_2/SnO_2 heterostructured nanoplates (HNPs). Benefiting from the unique structural features, the as-prepared SnS_2/SnO_2 HNPs exhibit significantly enhanced visible-light-driven photocatalytic activity in the reduction of aqueous Cr(VI).

Semiconductor hetero-nanostructures, composed of chemically distinct components, possess unique and enhanced properties in contrast with individual component materials, arising from strong interfacial interactions at the nanoscale, which have led to revolutionary new applications in various areas, such as catalysis, optical, magnetic, electrical, sensors, and so on.[1–9] As a kind of CdI_2-type layered semiconductor, SnS_2 displays a wide photoelectrochemical response in the visible light region with a narrow band gap of about 2.2 eV.[10,11] Compared with other metal sulfides, such as CdS, SnS_2 is low toxicity and good chemical stability makes it becomes a promising visible-light-driven photocatalyst.[12–14] SnO_2 is a stable oxide semiconductor with a wide band gap of about 3.5–3.8 eV, which can couple to SnS_2 to form a heterostructure for various potential applications, such as photocatalysis, gas-sensing, and lithium-ion batteries, *etc.*[15–17] Especially, SnS_2/SnO_2 hetero-nanostructures have demonstrated enhanced photocatalytic activity because of enhanced charge separation of photogenerated carriers through interfacial charge transfer.[15,16] Lots of research efforts have been devoted to the fabrication of this kind advantageous heterostructure.[17–19] However, to the best of our knowledge, there is no report on solution fabrication of SnS_2/SnO_2 heterostructures *via* an *in situ* hydrolysis process without employing any additional metal salt.

In this work, we have developed a controllable hydrothermal-assisted self-hydrolysis route to prepare SnS_2/SnO_2 heterostructured nanoplates (HNPs), which only use the pregrown SnS_2 nanoplates (NPs) as precursors without employing any additional surfactant. This is a facile and novel method, and a series of SnS_2/SnO_2 HNPs with the different SnO_2 contents have been successfully obtained by self-hydrolysis of SnS_2 NPs in the presence of citric acid at 180 °C for different time. A series of samples prepared with the different reaction time (0, 2, 5, 10, 14, and 24 h) in the hydrothermal process were denoted as pure SnS_2, H-2, H-5, H-10, H-14 and H-24, respectively. It has been discovered that the reaction duration plays a very important role in determining the size, morphology and composition of the final products. Benefiting from the unique structural features, the as-prepared SnS_2/SnO_2 HNPs exhibit significantly enhanced visible-light-driven photocatalytic activity in the reduction of aqueous Cr(VI). Furthermore, the mechanisms of the optimal SnO_2 content to reach the maximum photocatalytic activity in the SnS_2/SnO_2 HNPs are proposed and discussed.

The phase composition and structure of the as-prepared pure SnS_2 NPs and SnS_2/SnO_2 HNPs obtained with the different reaction times were first examined by powder X-ray diffraction (XRD) analysis, as shown in Fig. 1. For pure SnS_2 NPs, all the diffraction peaks can be well indexed to the pure hexagonal phase SnS_2 (JCPDS card no. 23-0677) with lattice constants of $a = 3.648$ Å and $c = 5.899$ Å. No impurity peaks are detected which shows that the products are of pure phase. For SnS_2/SnO_2 HNPs, in addition to the obvious SnS_2 patterns, broadened diffraction peaks at 2θ values of 26.6°, 33.9°, 37.9°, 51.8°, 54.8°, 57.8°, 61.9°, 64.7° and 65.9° match well with the (110), (101), (200), (211), (220), (002), (310), (112) and (301) crystal planes of tetragonal phase SnO_2 (JCPDS card no. 41-1445, $a = 4.738$ Å), respectively. In particular, the peak intensity of the SnO_2 component gets stronger with the increase of the hydrolysis time, indicating the amount of SnO_2 in the hybrid system is increased gradually. The energy dispersive X-ray spectroscopy (EDS) analysis was also

Key Laboratory of the Ministry of Education for Advanced Catalysis Materials, Institute of Physical Chemistry, Zhejiang Normal University, Jinhua, 321004, P. R. China. E-mail: yonghu@zjnu.edu.cn

† Electronic supplementary information (ESI) available: Detailed experimental procedures, additional EDS pattern, UV-vis diffuse reflectance spectra. See DOI: 10.1039/c4ra03943b

‡ These authors contributed equally to this work.

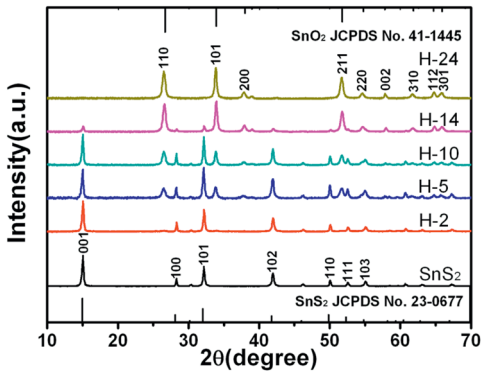

Fig. 1 XRD patterns of as-prepared pure SnS_2 NPs and SnS_2/SnO_2 HNPs obtained with different reaction durations.

performed to confirm the existence of Sn, O, and S elements in the hetero-nanostructures (Fig. S1, see ESI†). The SnS_2/SnO_2 moral ratio in the nanocomposites (Table S1, see ESI†) decreases with the increase of reaction time in the hydrothermal process, consistent with the XRD analysis.

The typical scanning electron microscopy (SEM) images of the as-obtained pure SnS_2 NPs and SnS_2/SnO_2 HNPs are shown in Fig. 2. A panoramic view of the SEM image (Fig. 2a) of pure SnS_2 shows that the product is completely composed of monodispersed hexagonal plates with an average size of around 500 nm in diameter. The high-magnification image (inset in Fig. 2a) reveals the surface of SnS_2 NP is relatively smooth, without the presence of any secondary nanostructures. Time-dependent experiments are carried out to understand the formation process of HNPs, Fig. 2b–f shows the SEM images of five samples obtained with different reaction durations in the self-hydrolysis process. As can be seen in Fig. 2b, at the early stage of the reaction (2 h), some particle subunits are formed on the surface of SnS_2 NPs. When the reaction duration is increased to 5–14 h (Fig. 2c–e), the product obviously contains a large portion of irregular particles deposited on the surface of NPs. And, the nanoparticles gradually grow into short nanorods with the increasing of reaction time. When the reaction duration is further prolonged, the SnS_2 NPs can hardly been observed due to the more Sn^{4+} ions released from SnS_2 (Fig. 2f).

Transmission electron microscopy (TEM) and high-resolution (HR)TEM measurements provide further information about the microstructure of the products. Fig. 3a shows typical TEM image of the as-prepared H-5 sample, where we can clearly see that monodispersed SnO_2 nanoparticles are tightly grown on the surface of the SnS_2 NP. The interface of SnS_2/SnO_2 hetero-nanostructure is further confirmed by the HRTEM image (Fig. 3b), the fringe interval of 0.28 nm corresponds to the interplanar spacing of the (101) planes of hexagonal phase SnS_2, while the 0.33 nm interval is in agreement with the (110) interplanar spacing of tetragonal phase SnO_2.

Based on all the above experimental results, the growth process of the SnS_2/SnO_2 HNPs is illustrated in Scheme 1. In an acidic solution, Sn^{4+} ions hydrolyze first and then further dehydrate to produce SnO_2 according to reactions 1 (eqn (1)) and 2 (eqn (2)) at 180 °C under hydrothermal treatment.[20,21]

$$Sn^{4+} + 4H_2O \rightarrow Sn(OH)_4 + 4H^+ \quad (1)$$

$$Sn(OH)_4 \rightarrow SnO_2 + 2H_2O \quad (2)$$

When the reaction time is prolonged, the successively released Sn^{4+} from the dissociation reactions of SnS_2 will further hydrolyze and nucleate to form SnO_2 nanoparticles on the surface of SnS_2 NPs. However, the-obtained SnO_2 nanoparticles with high-energy sites will further grow according to crystallographic-oriented direction to form short nanorods with the increasing of reaction duration.[5] Meanwhile, SnS_2 NPs are gradually dissolved to provide continuous Sn^{4+} ions for the growth of SnO_2 so that SnO_2 short nanorods are finally obtained while very little SnS_2 are left after 24 h in the hydrothermal treatment.

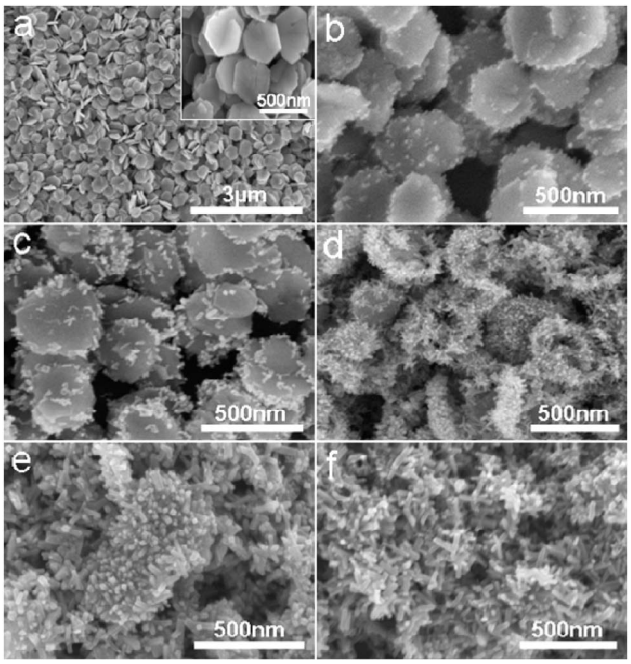

Fig. 2 SEM images of the as-obtained samples with the different reaction times: (a) pure SnS_2, (b) H-2, (c) H-5, (d) H-10, (e) H-14, and (f) H-24.

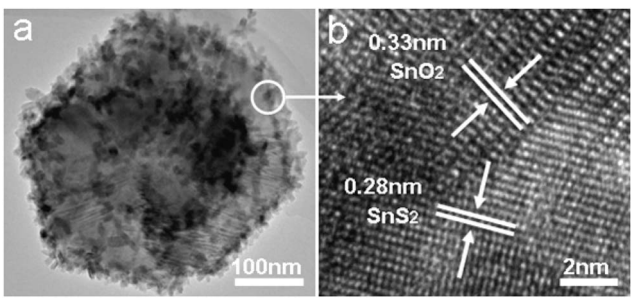

Fig. 3 (a) TEM and (b) HRTEM images of the as-obtained sample H-5.

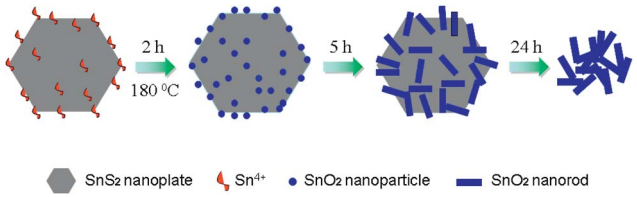

Scheme 1 Schematic illustration of the conversion processes from SnS_2 NP to SnS_2/SnO_2 HNP *via* a hydrothermal-assisted self-hydrolysis process.

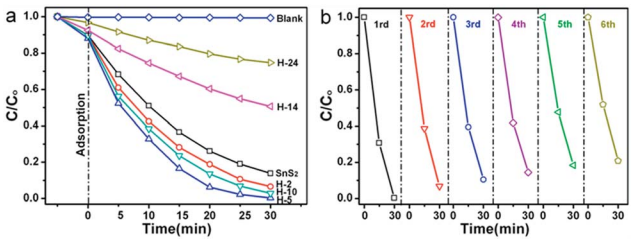

Fig. 4 (a) Photocatalytic reduction of Cr(VI) in the presence of different photocatalysts under visible-light irradiation. (b) Recycling test of photoreduction of Cr(VI) using sample H-5 as the photocatalyst under visible-light irradiation for 30 min.

The UV-vis diffuse reflectance spectra of the as-prepared pure SnS_2 NPs and SnS_2/SnO_2 HNPs are investigated (Fig. S2a, see ESI†). The pure SnS_2 NPs display optical absorption edge at around 550 nm, which may be assigned to the intrinsic bandgap absorption of SnS_2.[22] The absorption curves of the as-obtained sample H-2, H-5 and H-10 are similar to SnS_2 NPs, but the absorption intensity decreases with the less content SnS_2. For sample H-24, the sharp absorption onset at around 350 nm, corresponding to the big energy band gap of SnO_2 (3.5 eV),[23] which indicates that SnS_2 NPs are almost converted into SnO_2. The band gaps (E_g) of the samples are derived based on the theory of optical absorption using the relation (eqn (3)):[24]

$$(\alpha h\nu)^n = k(h\nu - E_g) \quad (3)$$

where $h\nu$ is the photon energy, α is the absorption coefficient, k is a constant relative to the material, and n is either 2 for a direct transition or 1/2 for an indirect transition. The E_g of the as-prepared pure SnS_2, H-2, H-5, H-10, H-14 and H-24 are estimated to be 2.23, 2.21, 2.21, 2.24, 2.24 and 3.51, respectively, which indicates that SnS_2/SnO_2 have the potential to be efficient visible light-driven photocatalysts (Fig. S2b, see ESI†). To further investigate the heterojunction interface is beneficial to photogenerated charge separation, the photocurrent transient response measurement of pure SnS_2 and SnS_2/SnO_2 heterostructure (sample H-5) is performed. Fig. S3 (see ESI†) shows the rapid and consistent photocurrent responses for each switch-on and -off event in multiple 100s on–off cycles under visible-light illumination. It is worth to note that the photocurrent density of the SnS_2/SnO_2 heterostructure is about 40 μA cm^{-2}, almost 4 times higher than that of pure SnS_2, which is about 10 μA cm^{-2}. The enhanced photocurrent response of the as-prepared SnS_2/SnO_2 heterostructure indicates higher separation efficiency of the photoinduced carriers and a lower recombination rate in such hybrid structures under visible-light illumination. This can be explained by the favorable transfer of electrons from SnS_2 to SnO_2 that reduces the recombination of electron–hole pairs. Therefore, the SnS_2/SnO_2 HNPs exhibit the enhanced photoreduction of Cr(VI).

The photocatalytic reduction tests of Cr(VI) species in an aqueous solution under visible-light irradiation using the as-prepared SnS_2/SnO_2 HNPs as photocatalysts were further carried out. As can be seen in Fig. 4a, where C is the concentration of Cr(VI) after light irradiation and C_0 is the initial concentration of Cr(VI) before dark adsorption. After irradiated for 30 min, there is no obvious change in the Cr(VI) concentration after visible-light irradiation in the absence of the catalysts, whereas nearly 86.2%, 93.4%, 99.7%, 97.2%, 49.4% and 25.3% of Cr(VI) is degraded by samples pure SnS_2, H-2, H-5, H-10, H-14 and H-24, respectively. The sample H-5 exhibits the highest photocatalytic activity among all of the samples, which indicates that there is an optimal loading amount of SnO_2 nanoparticles on the SnS_2 NPs. We have further studied the stability and reusability of sample H-5, as shown in Fig. 4b. After six cycles of photocatalytic reduction of Cr(VI), there is still 79.1% of Cr(VI) can be reduced. This loss might be mainly caused by the deposited Cr(III) species on the surface of SnS_2/SnO_2 HNPs,[12,25] and partly caused by the loss of the photocatalysts during each collection and rinsing cycle. The superior photocatalytic reduction activity of these hetero-nanostructures may be ascribed as follows. A schematic diagram representing charge transfer process in the SnS_2/SnO_2 HNPs is illustrated in Scheme S1 (see ESI†). The conduction band of SnS_2 is more negative than that of SnO_2, the electrons quickly transfer to the conduction band of SnO_2 when SnS_2 is excited under visible-light illumination, whereas the generated holes accumulate in the valence band of SnS_2. The efficient separation of the electron–hole pairs and reduction of charge recombination in the electron transfer process increases both the yield and the lifetime of the photogenerated carriers, and consequently enhances the photocatalytic performance. However, the excessive SnO_2 may reduce the inherent optical absorption of SnS_2 and result in a rapid decrease in photogenerated charges, ultimately reducing the photocatalytic activity. Therefore, the sample H-5 should have the ideal hetero-nanostructure, which possess the optimal balancing of charge separation and transport and hence demonstrate most favorable photocatalytic reduction activity in this particular case. The surface area of the as-prepared pure SnS_2 and SnS_2/SnO_2 HNPs (sample H-5 and H-24) is measured by the Brunauer–Emmett–Teller (BET) method using an ASAP2020 sorptometer. The as-prepared pure SnS_2, H-5, and H-24 have a specific surface area of 12.16, 15.93 and 27.94 m^2 g^{-1}, respectively. This result indicates that the surface areas of the as-obtained products gradually increase when the self-hydrolysis reaction time is prolonged. Thus, the specific surface area is not the determining factor in the photocatalytic efficiency.

In summary, we have developed a facile hydrothermal-assisted self-hydrolysis route to form SnS_2/SnO_2 HNPs, which only use the as-obtained SnS_2 NPs as precursors in the presence of citric acid. It has been found that the size, morphology and content of SnO_2 in the SnS_2/SnO_2 HNPs can be conveniently tuned by just varying the reaction duration in the hydrothermal treatment. As expected, the as-prepared SnS_2/SnO_2 HNPs exhibit enhanced visible-light-driven photocatalytic activity in the reduction of aqueous Cr(VI), because the interfacial electron can transfer from SnS_2 to SnO_2 in the SnS_2/SnO_2 hybrid system. The synthetic method presented here is very simple and cost-effective, and can be extended to prepare other metal sulfide/oxide hetero-nanostructures for a wide range of applications.

Acknowledgements

Y. Hu acknowledges financial support from the Natural Science Foundation of China (21171146, 21371152) and Zhejiang Provincial Natural Science Foundation of China (LR14B010001).

Notes and references

1 Y. R. Wang, W. L. Yang, L. Zhang, Y. Hu and X. W. Lou, *Nanoscale*, 2013, **5**, 10864–10867.
2 H. Y. Zheng, Y. J. Li, H. B. Liu, X. D. Yin and Y. L. Li, *Chem. Soc. Rev.*, 2011, **40**, 4506–4524.
3 W. L. Yang, L. Zhang, Y. Hu, Y. J. Zhong, H. B. Wu and X. W. Lou, *Angew. Chem., Int. Ed.*, 2012, **51**, 11501–11504.
4 X. H. Zhao, P. Wang and B. J. Li, *Chem. Commun.*, 2010, **46**, 6768–6770.
5 Z. Lou, F. Li, J. N. Deng, L. L. Wang and T. Zhang, *ACS Appl. Mater. Interfaces*, 2013, **5**, 12310–12316.
6 L. Y. Mao, Y. R. Wang, Y. J. Zhong, J. Q. Ning and Y. Hu, *J. Mater. Chem. A*, 2013, **1**, 8101–8104.
7 D. Sarkar, G. G. Khan, A. K. Singh and K. Mandal, *J. Phys. Chem. C*, 2012, **116**, 23540–23546.
8 Y. Hu, H. H. Qian, Y. Liu, G. H. Du, F. M. Zhang, L. B. Wang and X. Hu, *CrystEngComm*, 2011, **13**, 3438–3443.
9 B. Mukherjee, A. Peterson and V. Subramanian, *Chem. Commun.*, 2012, **48**, 2415–2417.
10 Y. F. Sun, H. Cheng, S. Gao, Z. H. Sun, Q. H. Liu, Q. Liu, F. C. Lei, T. Yao, J. F. He, S. Q. Wei and Y. Xie, *Angew. Chem., Int. Ed.*, 2012, **51**, 8727–8731.
11 P. Chen, Y. Su, H. Liu and Y. Wang, *ACS Appl. Mater. Interfaces*, 2013, **5**, 12073–12082.
12 Y. C. Zhang, J. Li, M. Zhang and D. D. Dionysiou, *Environ. Sci. Technol.*, 2011, **45**, 9324–9331.
13 X. Li, J. Zhu and H. X. Li, *Appl. Catal., B*, 2012, **123–124**, 174–181.
14 Z. Y. Zhang, C. L. Shao, X. H. Li, Y. Y. Sun, M. Y. Zhang, J. B. Mu, P. Zhang, Z. C. Guo and Y. C. Liu, *Nanoscale*, 2013, **5**, 606–618.
15 X. L. Zhou, T. F. Zhou, J. C. Hu and J. L. Li, *CrystEngComm*, 2012, **14**, 5627–5633.
16 Y. C. Zhang, Z. N. Du, K. W. Li, M. Zhang and D. D. Dionysiou, *ACS Appl. Mater. Interfaces*, 2011, **3**, 1528–1537.
17 K. Chang, W. X. Chen, H. Li and H. Li, *Electrochim. Acta*, 2011, **56**, 2856–2861.
18 Y. C. Zhang, L. Yao, G. Zhang, D. D. Dionysiou, J. Li and X. Du, *Appl. Catal., B*, 2014, **144**, 730–738.
19 Y. C. Zhang, Z. N. Du and M. Zhang, *Mater. Lett.*, 2011, **65**, 2891–2894.
20 Z. Y. Wang, Z. C. Wang, S. Madhavi and X. W. Lou, *Chem.–Eur. J.*, 2012, **18**, 7561–7567.
21 Z. H. Wen, G. Wang, W. Lu, Q. Wang, Q. Zhang and J. H. Li, *Cryst. Growth Des.*, 2007, **7**, 1722–1725.
22 R. Lucena, F. Fresno and J. C. Conesa, *Appl. Catal., A*, 2012, **415–416**, 111–117.
23 C. H. Wang, C. L. Shao, X. T. Zhang and Y. C. Liu, *Inorg. Chem.*, 2009, **48**, 7261–7268.
24 C. Y. Yu, Y. R. Wang, Y. Liu, C. F. Guo and Y. Hu, *Mater. Lett.*, 2013, **100**, 278–281.
25 N. Wang, Y. Z. Xu, L. H. Zhu, X. T. Shen and H. Q. Tang, *J. Photochem. Photobiol., A*, 2009, **201**, 121–127.